Indian Journal of Chemical Technology
Vol. 32, July 2025, pp. 466-477
DOI: 10.56042/ijct.v32i4.15958

Modeling of magnetohydrodynamic Casson nanofluid flow with nonlinear thermal radiation in a stretching porous channel using ANN and Levenberg–Marquardt optimization

Aghalya T[1], Tamizharasi R[2]* & Balakrishnama Manohar[1]

[1]Department of Mathematics and Statistics, School of Applied Science and Humanities, Vignan's Foundation for Science, Technology and Research, Vadlamudi, Guntur–522213, Andhra Pradesh, India

[2]Department of Mathematics, School of Advanced Sciences, Vellore Institute of Technology, Vellore- 632 014, Tamil Nadu, India

*E-mail: tamizharasi.r@vit.ac.in

Received 26 December 2024; accepted 13 June 2025

This study presents a computational approach to investigate the impact of nonlinear thermal radiation on the magnetohydrodynamic (MHD) flow of Casson nanofluids (Ag/H_2O and CuO/H_2O) over an expanding wall within a permeable path, considering heat generation/absorption and suction effects. The governing partial differential equations (PDEs) are transformed into nonlinear ordinary differential equations (ODEs) using a similarity transformation and are numerically solved via the Runge-Kutta method with the shooting technique. As a key novelty, an artificial neural network (ANN) model utilizing Levenberg-Marquardt (LM) optimization is developed to enhance predictive accuracy by integrating heat-related factors and the solid volume fraction. The graphical analysis of numerical results illustrates how key parameters influence velocity, temperature, skin friction and the Nusselt number. Comparisons with existing literature confirm the high accuracy of predicting skin friction coefficients and heat transfer rates. The ANN-LM model achieves R-values very close to one across all response variables, indicating strong model performance. Overall, the study results demonstrate that the developed ANN-LM model is highly accurate in predicting skin friction coefficients and the Nusselt number. The findings highlight the significant role of nonlinear thermal radiation in optimizing nanofluid-based cooling systems, with potential applications in biomedical engineering, electronics cooling and energy transport technologies.

Keywords: Artificial Neural Network, Casson nanofluid, Heat generation/absorption, Levenberg-Marquardt, Magnetohydrodynamic, Porous channel, Thermal Radiation

Introduction

Nanofluids, introduced by Choi and Eastman[1], are heat transfer fluids containing nanoparticles dispersed in base fluids like water or oils. These nanoparticles enhance thermal conductivity and improve both conduction and convection, making nanofluids highly effective in applications such as solar heating, nuclear cooling, electronics, heat exchangers, and thermal storage. For detailed reviews, Wang and Mujumdar[2], Wen et al.[3], Wong and Leon[4], and Saidur et al.[5] may be referred. Casson nanofluids are formed by adding nanoparticles to Casson fluids, which are non-Newtonian and exhibit yield stress with nonlinear stress–strain behaviour. These fluids require a threshold stress to initiate flow and show varying viscosity with shear rate[6]. Studies by Khan et al.[7,8] explored the effects of nonlinear heat emission, MHD and electric fields on complex nanofluid flows involving thermal and radiative influences. Pop et al.[9] numerically analyzed Casson fluid flow in a square cavity, showing that thermal transfer increases with higher Casson parameter values. Mythili et al.[10] studied heat generation and absorption effects on Casson fluid flow over a vertical cone and horizontal surface, highlighting their significant influence on heat transfer.

Mukhopadhyay[11] studied unsteady flow and heat transfer over a porous stretching surface within a porous channel. Chamkha[12], using the finite volume method, found that internal heat generation reduces the mean Nusselt number in electrically conducting fluids. Saleem et al.[13] analyzed heat and mass transfer in MHD Jeffrey fluid flow over a rotating cone with a heat source and chemical reaction using the Optimal Homotopy Analysis Method.

Sheikholeslami et al.[14] found that applying a magnetic field to CuO nanofluids enhances heat transfer. Gireesha et al.[15] numerically studied Casson nanofluid flow with exponential heat sources,

activation energy, and chemical reactions, noting higher Nusselt numbers for nonlinear radiation. Dharmaiah et al.[16] used perturbation methods to analyze silver (Ag)–water (H_2O) nanofluid behaviour by solving nonlinear ODEs. Nouri et al.[17] applied Differential Transformation and Least Square Methods in their analysis. Aghalya et al.[18] provided a computational study on MHD flow and thermal radiation of Casson nanofluids in a permeable expanding channel. Varatharaj and Tamizharasi[19] examined nonlinear thermal radiation effects on Cu-H_2O and TiO_2-H_2O Casson nanofluids over a stretching wall, using the Runge-Kutta method with a shooting technique.

Raja et al.[20] used Bayesian Regularization with backpropagation neural networks to model 3D hybrid nanofluid flow with radiative heat and mass transfer. Davood et al.[21] developed an ANN to predict the viscosity of Ag/ethylene glycol nanofluids. Akhgar et al.[22] designed ANNs for predicting thermal conductivity of MWCNT-TiO_2/water-ethylene glycol nanofluids. Anil Kumar et al.[23] applied the Levenberg–Marquardt algorithm to optimize entropy in Casson hybrid nanofluid flow with nonlinear thermal radiation.

The study investigates the combined effects of heat generation/absorption and thermal radiation. By applying similarity transformations, the researchers transformed the momentum and energy equations into ordinary differential equations, which were then numerically simulated with precision by adjusting dimensionless parameters within the problem. The results were thoroughly analyzed, demonstrating that factors like parallel flow have a notable impact on flow behaviour and heat transfer. Additionally, the study emphasizes a significant industrial application: accurately estimating skin friction and the Nusselt number, which holds relevance for electronic devices that produce substantial heat and thus depend on efficient heat management for reliable performance. Examining electronic connections is therefore essential for enhancing circuit performance in nearby areas. To solve these equations, the RK-4 method was integrated with a shooting technique and artificial neural networks (ANN) to improve accuracy and reliability. Data sets were divided into training, testing and validation groups, utilizing backpropagation and the Levenberg–Marquardt (LM) algorithm. Regression analysis, along with the best validation performance and error histograms, confirmed the robustness of the results. The effects of various physical parameters on skin friction and the Nusselt number were further analyzed and presented in both graphical and tabular formats, with comparisons to configurations over parallel channels.

Mathematical Representation

We examine a situation involving a consistent, smooth and incompressible flow of a nanofluid with electrical conductivity, following the Casson model, within a semi-porous channel. This scenario has been previously explored by Nouri[17] and colleagues in their research. A cartesian position plane is utilized, where the $\hat{x}$-axis aligns with the flow direction and the $\hat{y}$-axis is orthogonal to the channel's orientation. The top wall is considered to be located at $\hat{y}$= a and it is stationary and impermeable. On the other hand, the bottom wall is situated at $\hat{y}$= −a. This bottom wall is both porous and capable of elongating in the direction of $\hat{x}$-axis, as depicted in Fig. 1. The stream experiences a consistently applied magnetic field, denoted as B_0, aligned with the $\hat{y}$-axis direction. The equations that govern the behaviour of the described fluid model are presented[17, 18, 19] as follows:

$$\frac{\partial \hat{u}}{\partial \hat{x}} + \frac{\partial \hat{v}}{\partial \hat{y}} = 0 \quad \ldots (1)$$

$$\rho_{nf}\left(\hat{u}\frac{\partial \hat{u}}{\partial \hat{x}} + \hat{v}\frac{\partial \hat{u}}{\partial \hat{y}}\right) = \mu_{nf}\left(1+\frac{1}{\beta_c}\right)\frac{\partial^2 \hat{u}}{\partial \hat{y}^2} - \left(\sigma_{nf}B_0^2 + \frac{\mu_{nf}}{k_0}\right)\hat{u} - \frac{\partial \hat{p}}{\partial \hat{x}} \quad \ldots (2)$$

$$\rho_{nf}\left(\hat{u}\frac{\partial \hat{v}}{\partial \hat{x}} + \hat{v}\frac{\partial \hat{v}}{\partial \hat{y}}\right) = \mu_{nf}\left(1+\frac{1}{\beta_c}\right)\frac{\partial^2 \hat{v}}{\partial \hat{x}^2} - \frac{\partial \hat{p}}{\partial \hat{y}} \quad \ldots (3)$$

$$\left(\hat{u}\frac{\partial \hat{T}}{\partial \hat{x}} + \hat{v}\frac{\partial \hat{T}}{\partial \hat{y}}\right) = \frac{k_{nf}}{(\rho C_p)_{nf}}\frac{\partial^2 \hat{T}}{\partial \hat{y}^2} - \frac{1}{(\rho C_p)_{nf}}\frac{\partial q_r}{\partial \hat{y}} - \frac{Q_0}{(\rho C_p)_{nf}}(\hat{T} - \hat{T}_\infty) \quad \ldots (4)$$

The given information pertains to a situation where $\hat{u}$ and $\hat{v}$ represent the speed vectors in the $\hat{x}$ and $\hat{y}$ paths.

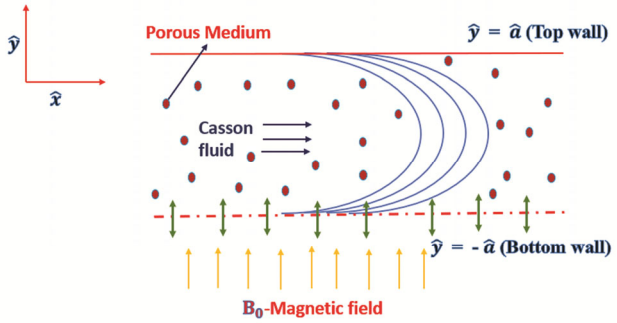

Fig. 1 — Physical Geometry

The suitable initial and boundary conditions are provided as follows:

$\hat{u}= \hat{b}\hat{x}$, $\hat{v}$ = -v_0, $\hat{T} = \hat{T}_1$ at $\hat{u}$= -$\hat{a}$ … (5)

$\hat{u}$= 0, $\hat{v}$ = 0, $\hat{T} = \hat{T}_\infty$ at $\hat{u}= \hat{a}$ … (6)

When working with a channel in which the walls can either contract ($\hat{b}$< 0) or expand ($\hat{b}$> 0).

Therefore, the Rosseland approximation[24] is suitable for describing the radiative heat flux q_r in this context.

$$q_r = -\frac{4\sigma^*}{3k^*}\frac{\partial \hat{T}^4}{\partial \hat{y}} \quad \dots (7)$$

Temperature variations within the flow are assumed to be relatively small $\hat{T}_\infty^4$ can be approximated as a linear function of temperature. This simplification is achieved by disregarding higher-order terms and using an expanded Taylor series representation of $\hat{T}_\infty$.

$$-3\hat{T}_\infty^4 + 4\hat{T}_\infty^3 = \hat{T}^4 \quad \dots (8)$$

Therefore, it is obtained as,

$$\frac{\partial q_r}{\partial \hat{y}} = -\frac{16\sigma^*}{3k^*}\hat{T}_\infty^3\frac{\partial^2 \hat{T}}{\partial \hat{y}^2} \quad \dots (9)$$

From eqns. (2.7) to (2.9), eqn. (2.4) reduces to,

$$\left(\hat{u}\frac{\partial \hat{T}}{\partial \hat{x}} + \hat{v}\frac{\partial T}{\partial \hat{y}}\right) = \frac{k_{nf}}{(\rho C_p)_{nf}}\frac{\partial^2 \hat{T}}{\partial \hat{y}^2} - \frac{16\sigma^*}{(\rho C_p)_{nf}3k^*}\hat{T}_\infty^3\frac{\partial^2 \hat{T}}{\partial \hat{y}^2} - \frac{Q_0}{(\rho C_p)_{nf}}(\hat{T} - \hat{T}_\infty) \quad \dots (10)$$

Addressing the Problem

Table S1 (Supplementary Information) shows that the thermodynamic characteristics of nanofluids. We used the following similarity transformations to derive ordinary differential equations:

$$x^* = \frac{\hat{x}}{\hat{H}}, y^* = \frac{\hat{y}}{\hat{H}}, \hat{u} = -\nu\, x^* f'(y^*),$$
$$\hat{v} = \nu f(y^*), \theta = \frac{\hat{T}-\hat{T}_\infty}{\hat{T}_1-\hat{T}_\infty} \quad \dots (11)$$

Through the use of similarity variables, eqns. (1) to (4) have been converted or transformed as follows:

$$f'^v = \frac{(f'f'' - ff''')J_1JR_N(1-\phi)^{2.5} + f''(J_4M^2(1-\phi)^{2.5} + K_r)}{\left(1+\frac{1}{\beta_c}\right)} \quad \dots (12)$$

$$\theta'' = -\frac{J_2 Pr}{N+J_3}[f\theta' + H_T\theta] \quad \dots (13)$$

where

$R_N = \frac{\nu H}{\nu f}$ (Stretching Reynolds number),

$Pr = \frac{\nu H(\rho C_p)_f}{k_f}$ (Prandtl number),

$M^2 = \frac{\sigma B_0^2 H^2}{\mu_f}$ (Hartmann number),

$N = \frac{16\sigma^*}{k_f 3k^*}\hat{T}_\infty^3$ (Thermal radiation number),

$H_T = \frac{Q_0 H}{\nu(\rho C_p)_f}$(Heat source/sink parameter),

$K_r = \frac{\nu_f}{\nu k_0}$(Porosity parameter),

Also,

$$J_1 = \frac{\rho_{nf}}{\rho_f} = (1-\phi) + \frac{\rho_{nf}}{\rho_f}\phi$$

$$J_2 = \frac{(\rho C_p)_{nf}}{(\rho C_p)_f} = \frac{(\rho C_p)_s}{(\rho C_p)_f}\phi + (1-\phi)$$

$$J_3 = \frac{k_{nf}}{k_f} = \frac{(k_s + 3k_f - k_f) - 2\phi(k_f - k_s)}{(k_s + 3k_f - k_f) + 2\phi(k_f - k_s)}$$

$$J_4 = \frac{\sigma_{nf}}{\sigma_f} = 1 + \left(\frac{3\left(\frac{\sigma_s}{\sigma_f} - 1\right)\phi}{\left(\frac{\sigma_s}{\sigma_f} + 2\right) - \left(\frac{\sigma_s}{\sigma_f} - 1\right)\phi}\right)$$

The non-dimensional boundary conditions are taken into consideration:

$$f'(-1) = 1,\ f'(-1) = 0, \theta(-1) = 1 \quad \dots (14)$$

$$f(-1) = \lambda, f(1) = 0, \theta(-1) = 0 \quad \dots (15)$$

Where, λ is the suction parameter.

Physical Quantities

The important external factors of interest are the friction drag (τ) and local Nusselt number (Nu) is discussed by[28] and clearly stated as follows,

$$\tau = \frac{1}{\rho f}\left(\frac{\tau_w}{u_w^2}\right),\ Nu_x = x\left(\frac{q_w}{(T_w - T_\infty)k_f}\right) \quad \dots (16)$$

Where, τ_w and $q_w$represent the friction drag and the heat flux, respectively, given by,

$$\tau_w = \left(1 + \frac{1}{\beta_c}\right)\mu_{nf}\left(\frac{\partial \hat{u}}{\partial \hat{y}}\right)_{\hat{y}=0},\ q_w = k_{nf}\left(\frac{\partial \hat{T}}{\partial \hat{y}}\right)_{\hat{y}=0} \quad \dots (17)$$

With the help of Eqs. (16) and (17),

$$\tau(R_{N_x})^{\frac{1}{2}} = \left(1 + \frac{1}{\beta_c}\right)\left(\frac{f''(0)}{(1-\phi)^{2.5}}\right) \quad \dots (18)$$

$$Nu_x(R_{N_x})^{\frac{1}{2}} = -\frac{k_{nf}}{k_f}(1+N)\theta'(0) \quad \dots (19)$$

Numerical Solutions using RK-4 Method within the Shooting Technique

The problem of modelling the flow of the proposed nanofluid, as described from Eqs (1-4), inherently involves non-linearity. A numerical method is employed to obtain an approximate solution to the problem, combining the Runge-Kutta method. This approach necessitates the transformation of higher-order derivatives into first-order derivatives in the following manner:

$$\begin{bmatrix} f \\ f' \\ f'' \\ f''' \\ f^{'v} \\ \theta \\ \theta' \\ \theta'' \end{bmatrix} = \begin{bmatrix} f(1) \\ f(2) \\ f(3) \\ f(4) \\ f(4)' \\ f(5) \\ f(6) \\ f(6)' \end{bmatrix} \quad \ldots (20)$$

Finally, the converted 1st-order initial value problem is presented as

$$f(4)' = \left[J_1 R_N (1-\phi)^{2.5}\left(f(2)f(3) - f(1)f(4)\right) + \right.$$
$$\left. (J4M21 - \phi 2.5 + Kr) f(3) \beta c1 + \beta c \right. \quad \ldots (21)$$

$$f(6)' = \frac{J_2 Pr}{N + J_3}\left[f(1)f(6) + H_{Tf(5)}\right] \quad \ldots (22)$$

Eqs. (21) and (22) with respect to boundary conditions described in Eqs. (14) & (15) are addressed through the application of the RK-4 method, incorporating shooting strategies. The iteration continues till a level of accuracy reaching 10^6 is achieved. To access more information, see[29-31].

ANN Model

Artificial Neural Networks, inspired by the human brain, consist of simple processing units and adaptive interconnections, functioning like a multi-processor system[34]. ANNs have input, hidden, and output layers connected by weighted links. During training commonly using the back-propagation algorithm[35] weights and biases are adjusted to minimize prediction errors. The multilayer perceptron (MLP), a feed-forward network with one or more hidden layers, is the most widely used ANN type[36]. Fig. 2 illustrates a back-propagation neural network (BPNN) with input nodes, hidden nodes, and output nodes, using the sigmoid activation function. The network computes outputs by activating nodes based on input and weights, then compares the result to experimental data using Mean Squared Error. Weight updates are guided by three learning methods, which propagate the error backward to refine weights and improve accuracy across training cycles.

ANN training algorithms

This study employs the Levenberg-Marquardt algorithm as the learning method in ANNs, aiming to evaluate its speed and accuracy for the given application. The primary goal is to minimize global error, the difference between predicted and actual outputs by iteratively adjusting weights and biases. Using the ANN-LM method[37-40], outputs were computed from input data based on node activations and interconnection weights. These outputs were compared with experimental results to calculate the mean percentile error, which was then back-propagated to update weights. This process continued until the error dropped below a set threshold. As shown in Fig. 3, nine input parameters were used, with two outputs corresponding to *Nu* and τ.

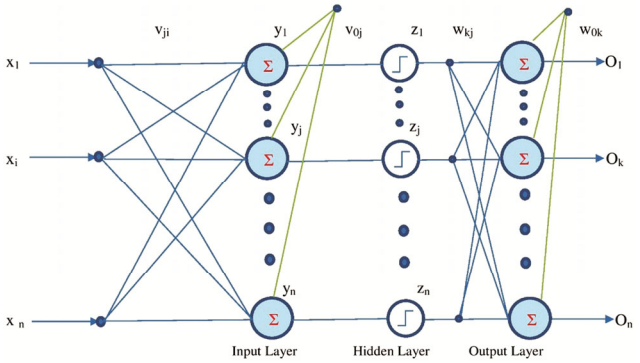

Fig. 2 — Artificial Neural Network with Back Propagation Algorithm

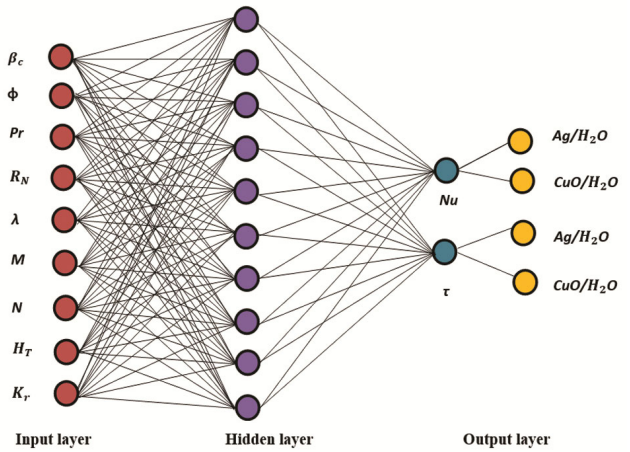

Fig. 3 — Schematic diagram of the proposed ANN model

Results and Discussion

The thermophysical properties characteristics of this nanofluid are displayed in Table 1. The findings are showcased using both tables and visual representations, enabling a thorough examination. Our main goal is to investigate numerical resolutions for the specified issue, taking into account different physical variables.

The impact of dimensionless parameters (β_c, λM, K_r, ϕ, N, H_T, R_N and Pr) on velocity and temperature in Ag/H_2O and CuO/H_2O Casson nanofluids re discussed in the proceeding sections. The visual depictions enable a visual comprehension of the data, emphasizing trends, patterns, and possible relationships. The integration of both tables and visual charts aids in achieving a thorough grasp of the numerical findings, empowering us to make well-informed choices and derive significant insights.

Effects of Solid Volume Fraction

Figs 4(a) and 4(b) illustrate the impact of ϕ on the velocity and temperature distributions in Ag/H_2O and CuO/H_2O Casson nanofluids. It can be deduced from Fig. 4(a) that as ϕ increases, the boundary layer thickness of the flow decreases. The heightened solid fractional volume, the proportion of nano-sized particles in the fluid also rises, leading to a denser fluid. Consequently, both the momentum and the thickness of the boundary layer in the flow reduce. It is noteworthy to point out, based on Fig. 4(b), an increase in fractional volume causes the Ag/H_2O nanofluid to flow at lower pace compared to the CuO/H_2O nanofluid.

Effects of Casson fluid Parameter

Fig. 5 illustrates the effect of the Casson parameter β_c on velocity and temperature profiles. As shown in Fig. 5(a), increasing β_c decreases the fluid velocity due to enhanced resistance to flow. In Fig. 5(b), high β_c increases the fluid's viscosity (shear-thickening behaviour), which reduces fluid motion and expands the momentum boundary layer. Between the two nanofluids, Ag/H_2O exhibits a thicker momentum boundary layer and absorbs more heat from the surface compared to CuO/H_2O, mainly due to its higher viscosity.

Effects of Porosity Parameter (K_r)

The impact of the permeability variable (K_r) on momentum and energy profiles is presented in Fig. 6. As depicted in Fig. 6(a), it is evident that the velocity field decreases with higher values of the porosity parameter. Notably, the velocity of Ag/H_2O nanofluid is only slightly lower than that of Ag/H_2O nanofluid. In Fig. 6(b), the influence of the porosity parameter Kr on the temperature profile is illustrated. It is observed that an increase in the value of the porosity parameter is directly associated with a rise in the fluid temperature.

Table 1 — Thermophysical characteristics[32] of H_2O and Ag & CuO nanoparticles

	$\rho\ (kg/m^3)$	$C_p\ (J/kgK)$	$\beta\ (1/K)$	$k\ (W/mK)$	$\sigma\ (S/m)$
Water (H_2O)	997.1	4179	$21x10^{-5}$	0.613	$5.5x10^{-6}$
Silver (Ag)	10500	235	$1.89x10^{5}$	429	$62.1x10^{6}$
Copper oxide (CuO)	6320	531.8	$1.80x10^{-5}$	76.5	$59.6x10^{-6}$

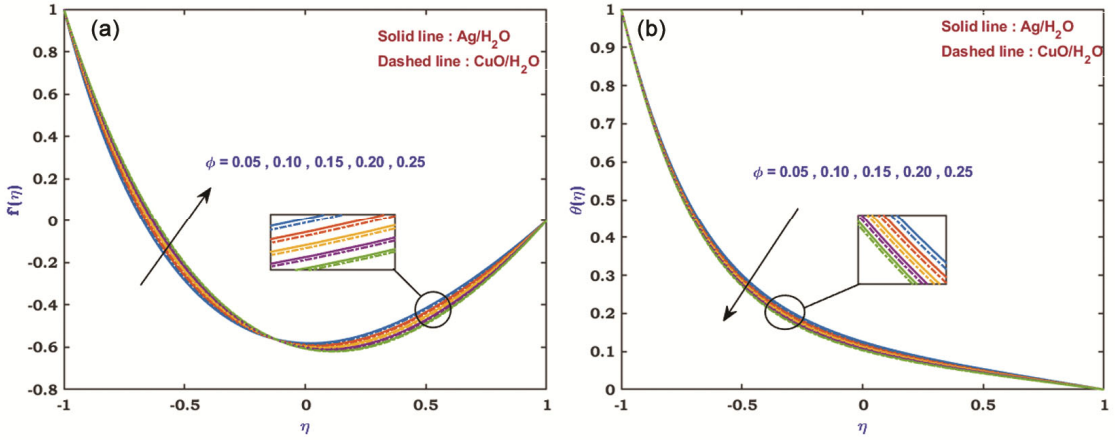

Fig. 4 — Impacts of ϕ on (a) velocity and (b) temperature

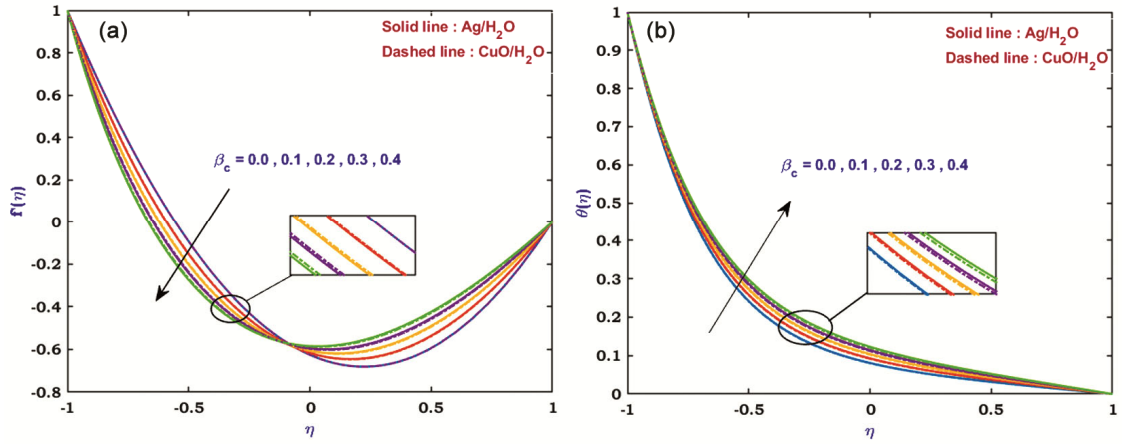

Fig. 5 — Impacts of β_c on (a) velocity and (b) temperature

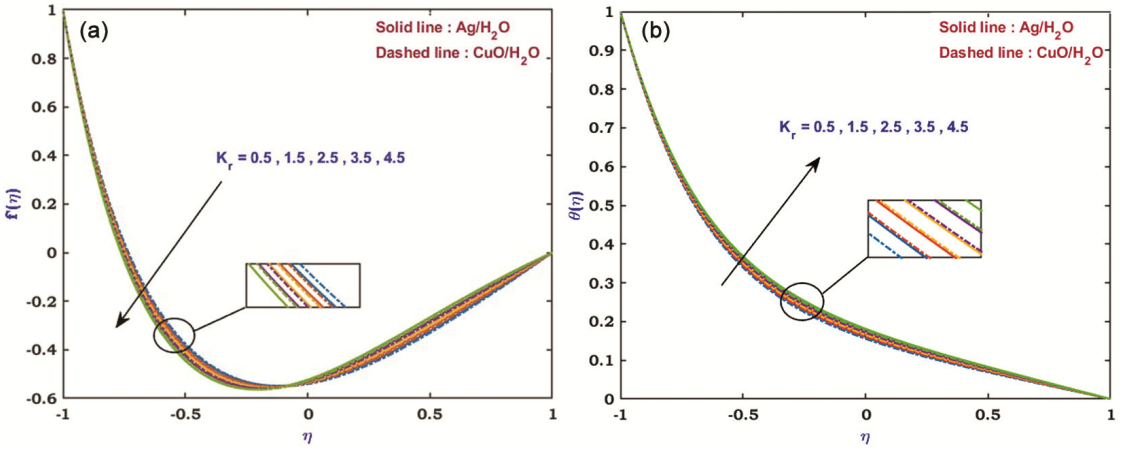

Fig. 6 — Impacts of K_r on (a) and (b) temperature

Effects of Hartmann Number(M)

The impact of the M on velocity and temperature distributions is demonstrated in Fig. S1 (Supplementary Information). Fig. S1 (a) shows that increase in M value reduces fluid velocity and thins the momentum boundary layer due to the opposing Lorentz force and also resulted in thinning the momentum boundary layer. Ag/H_2O exhibits higher velocity than CuO/H_2O. In contrast, temperature and thermal boundary layer thickness increase with MMM, as seen in Fig. S1(b).

Effects of Reynolds Number (R_N)

Fig. S2 illustrates how the R_N, controls the patterns of velocity and temperature distributions. In Casson nanofluid systems, an increase in the Reynolds number (R_N) typically leads to higher flow velocities and a more even, less variable velocity profile, as opposed to a decreasing velocity profile. This behaviour is generally observed when the Reynolds number rises. If the density and velocity of the Ag/H_2O and CuO/H_2O nanofluids remain fairly consistent, the Reynolds number (R_N) can rise due to the reduction in dynamic viscosity with higher temperatures. The Reynolds number is directly linked to both the velocity and dynamic viscosity of a fluid, and it exhibits an inverse relationship with the fluid density.

Effects of Suction parameter (λ)

Fig. 7(a) depicts the outcomes of the λ on the velocity distribution. When suction is applied at the wall of the channel, it essentially pulls the fluid towards the wall, generating a decline in the flow velocity(momentum) close to the wall. In essence, higher suction values lead to a more pronounced slowing down of the fluid flow due to the increased removal of nanofluid from the channel by the suction process.

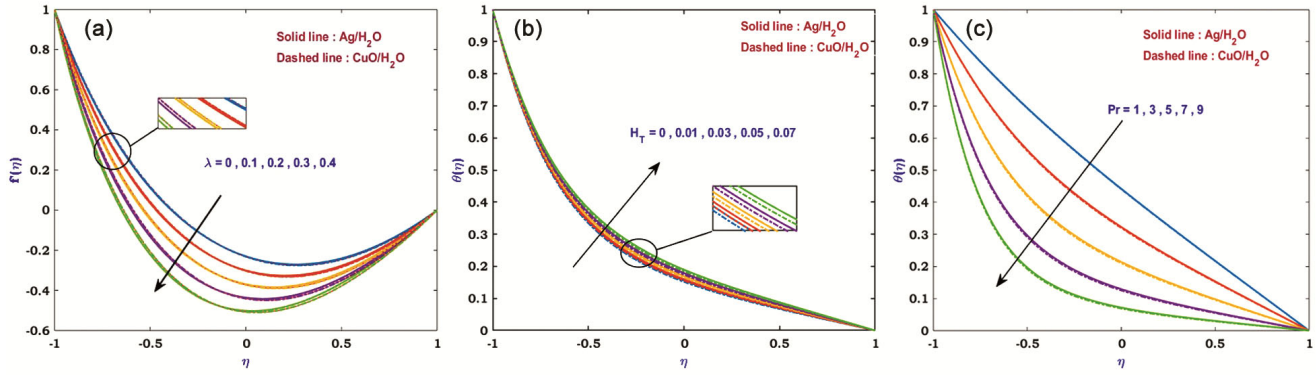

Fig. 7 — (a) Impacts of λ on velocity, (b) Impacts of H_T on temperature and (c) Impacts of Pr on temperature

Table 2 — Comparative study for Nusselt number with Pr = 1.0, N = 0.8, M = 0.4, λ = 0.5, R_N =10 and K_r= H_T = β_c = 0

ϕ	Raza et al.[33]	Varatharaj and Tamizharasi[19]	Present values of Nu	%Difference (w.r.t Raza et al.[33])	%Difference (w.r.t Varatharaj and Tamizharasi[19])
0	-0.709290125	-0.709	-0.70914	0.021%	0.019%
0.01	-0.694623691	-0.697	-0.69991	0.76%	0.42%
0.03	-0.668955131	-0.675	-0.67921	1.53%	0.62%
0.05	-0.647222635	-0.656	-0.64656	-0.10%	1.43%

Effects of Heat generation/absorption parameter (H_T)

Fig. 7(b) provide an analysis of how the temperature profile is influenced by the heat generation/absorption parameter (H_T). It demonstrates that when the heat generation/absorption parameter increases, the temperature also increases. This is due to the fact that a higher heat generation/absorption parameter contributes to heating the nanofluid, resulting in a noticeable temperature rise within the nanofluid.

Effects of Prandtl Number (*Pr*)

In Fig. 7(c), an increase in the Prandtl number (Pr), signifying a fluid with lower thermal diffusivity, results in a slight decrease in temperature across all points. A high Prandtl number indicates that heat is diffused more slowly compared to the momentum, meaning the fluid has relatively poor thermal conductivity. A higher Prandtl number in Casson nanofluids can result in a decreased temperature profile due to reduced thermal diffusivity within the fluid.

Investigation on skin friction and Nusselt number

Tables S2 - S5 (Supplementary Information) presents data on how different dimensionless factors, including the Reynolds number (R_N), Casson fluid parameter (β_c), Hartmann number (M), thermal radiation impact (N), presence of porous media (K_r), heat generation or absorption (H_T), suction variable (λ), Prandtl number (Pr), and solid volume fraction (ϕ), influence the levels of friction drag(Cf) and Nusselt number (Nu_x). When the solid volume fraction (ϕ) and the Casson fluid parameter (β_c) increase, the friction drag and heat transfer magnitudes decrease. Conversely, the Hartmann number(M) exhibits the opposite effect, leading to an increase in Cf and Nu_x. As the Pr, N, and H_T increase, friction drag remains constant in all three scenarios. However, heat transfer decreases for the cases associated with N and H_T and it increases for the case related to Pr. For suction parameter (λ) and porosity parameter (K_r) increasing, where friction drag decreases for increasing Nusselt number. There is down in Reynolds number (R_N), where sudden rise in both friction drag and Nusselt number, respectively.

Code Validation

The accuracy of the computational techniques is demonstrated using MATLAB software with the RK method. Through the MATLAB code style, the friction drag and Nusselt number are computed and presented in Table S5 for various values of relevant parameters, including β_c, Pr, N, M, λ. Similarly, applying to previous studies by (setting (H_T = K_r = 0) Raza et al.[33] and Varatharaj & Tamizharasi[19], the results align with the previously described findings and are presented in Table 2, covering a range of key parameter values. These consistent outcomes across both research cases demonstrate a high level of accuracy and agreement.

Analysis of an ANN model

The model uses parameters β_c, λ M, K_r, ϕ, N,H_T, R_N and Pr as inputs. Figures 3 and 5 show the ANN structures for predicting skin friction and Nusselt number, respectively. The ANN effectively captures the complex input-output relationships and shows strong agreement with computational results.

In this study, Tables 2, S2, S3 and S4 present the set values for β_c, λ M, K_r, ϕ, N, H_T, $R_N$and Pr for both skin friction (τ) and the Nusselt number (Nu). The numerical results obtained using the Runge–Kutta fourth-order method, shown in Tables S2 and S3, were used to train the ANN. The Levenberg–Marquardt backpropagation algorithm was employed for training the model. The parameters used in the ANN model are listed in supplementary Table S6.

The ANN model's predictions are in good agreement with the quantitative outcomes from classical methods. The results of this study suggest that the ANN can effectively predict both skin friction (τ) and the Nusselt number (*Nu*). The optimal number of nodes in the hidden layer was determined using a trial-and-error approach, based on the number of epochs required to train the network, ensuring that overfitting or underfitting was avoided and the training phase converged.

Through iterative processes, it was concluded that the best model configuration included a single hidden layer with five neurons. For the ANN model, 70% of the data were used for training, 15% for validation and the remaining 15% for testing the model's performance.

Best validation, error histogram and training performance

Figs 8, 9, S3, and S4 depict the ANN model's optimal performance invalidation, error histograms and training across all four scenarios.

- The plots of the Nusselt number and skin friction from the training scheme is displayed in Figs 8(a), 9(a), S3(a), and S4(a). Initially, the mean square error fluctuated unpredictably up until 7, 7, 8 and 6 epochs, respectively. However, after that point,

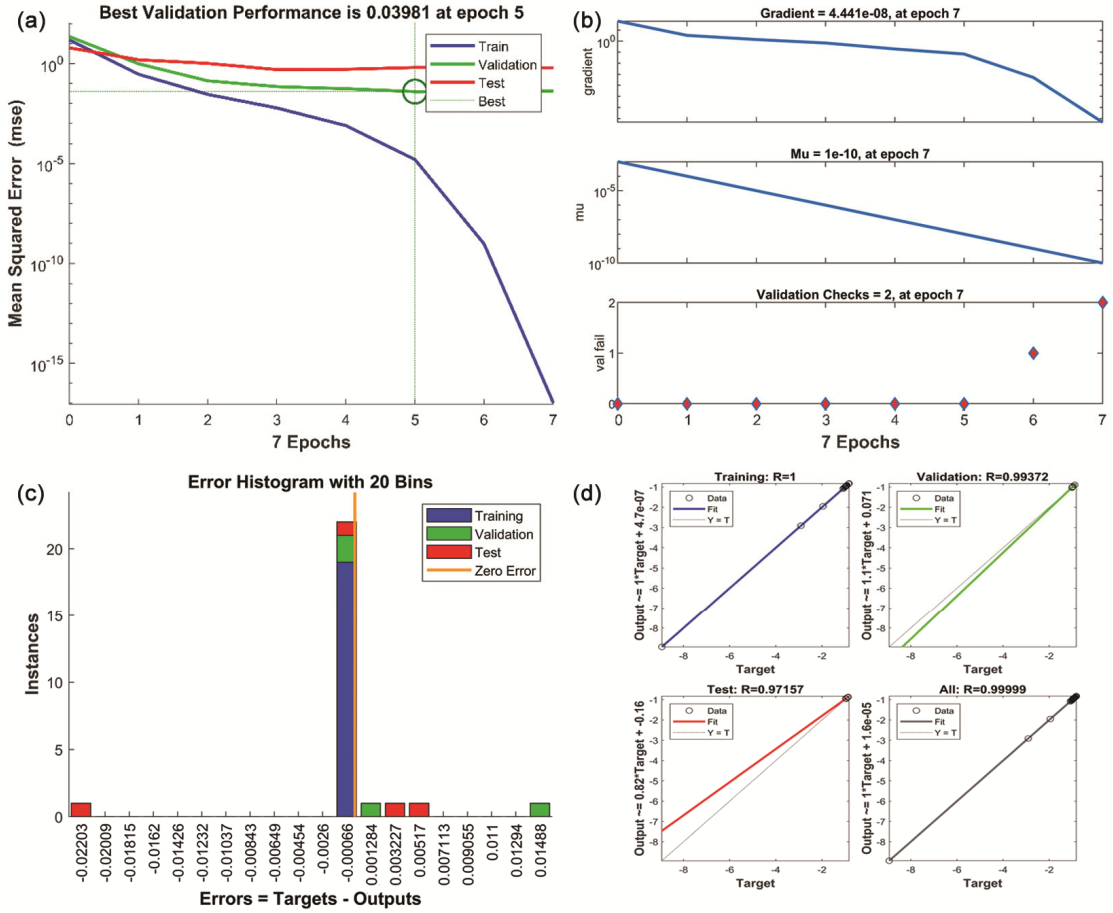

Fig. 8 — (a) Performance analysis, (b) training state, (c) error histogram and (d) regression analysis of Ag-H_2O

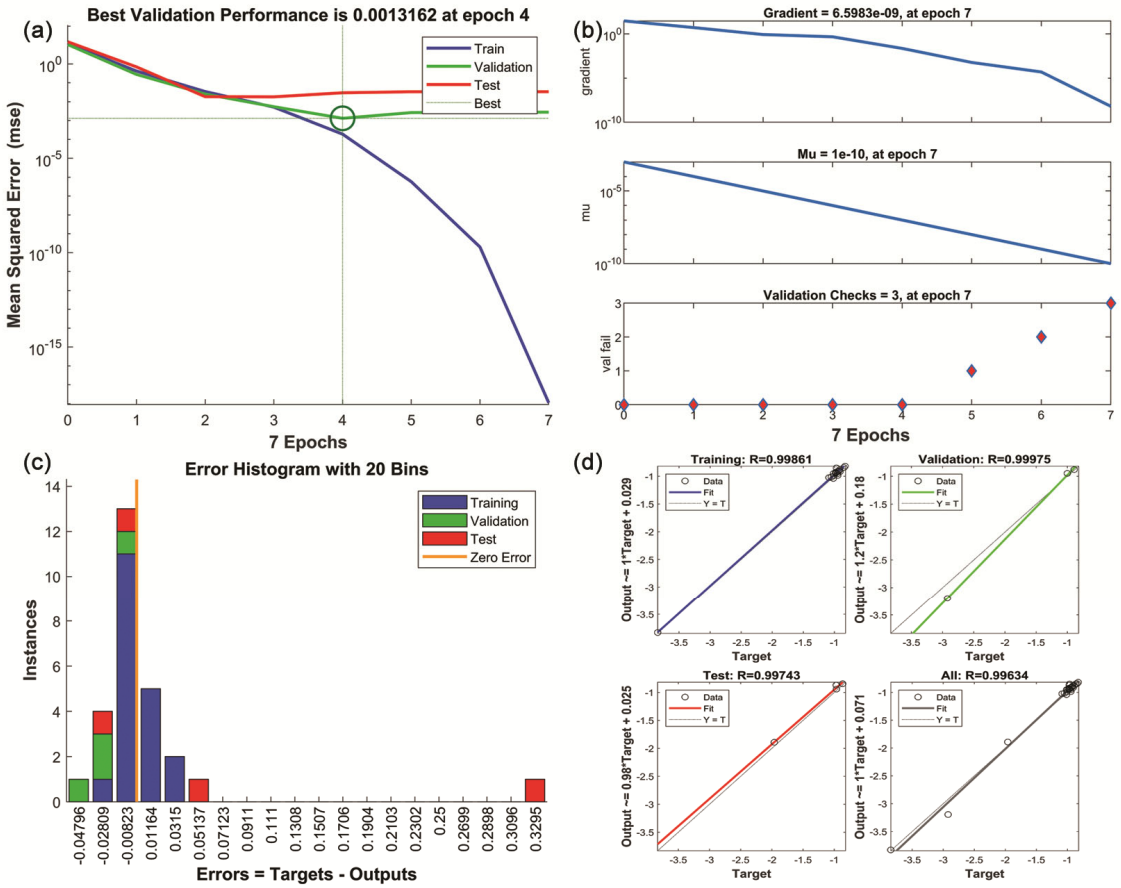

Fig. 9 — (a) Performance analysis, (b) training state, (c) error histogram and (d) regression analysis of CuO-H_2O

the best results were achieved across all bands in the following epochs. The optimal performance was reached with values of 0.03981 at epoch 5, 0.00131612 at epoch 4, 0.010651 at epoch 6 and 0.031524 at epoch 2, respectively.

- The gradient, Mu and validation parameters for the Bayesian regularization process are [4.441e-08, 1e-10, 2] and [6.5983e-09, 1e-10, 3] for *Nu*, as illustrated in Figs 8(b)and 9(b). Similarly, for τ, the gradient, Mu and validation parameters are [1.3847e-09, 1e-11, 2] and [1.2437e-14,1e-09,4], as shown in Supplementary Figs S3(b) and S4(b).
- **Error histogram**: The error histogram displays the distribution of errors between the target and predicted values after training a neural network, where errors may be negative, indicating deviations of predictions from actual values. For the ANN-LM model, Figs 8(c), 9(c) and S3(c), S4(c) use blue bars for training data, red bars for testing data, and green bars for validation data. The graph spans the error range (from the maximum negative to the maximum positive error) and is divided into 20 bins. This histogram helps identify out lier's data points where the model's fit significantly deviates from the rest of the dataset.
- Figs 8(c), 9(c), S3(c) and S4(c) present an error histogram highlighting the errors identified during the training phase of the ANN. The error values in this analysis are minimal compared to the values displayed along the x-axis of the histogram. These errors approach the zero-error line with values around -0.00066, -0.00823, -0.001662 and -0.01246 for *Nu* and τ, as estimated by the ANN model. An examination of the histogram, which visualizes error distribution across three different datasets, reveals that the errors are tightly grouped around the yellow line, which marks the zero-error threshold. This analysis of the error histogram clearly indicates that the ANN model's training phase was successfully completed, as demonstrated by the remarkably lower rate.

- **Regression Analysis:** The regression plots are instrumental in evaluating the network's performance by comparing its output to target values across training, validation, testing and overall datasets. For the ANN, the entire validation dataset contributes to the training process. In these plots, an R-value close to 1 indicates an ideal model fit, as illustrated in Figs 8(d), 9(d) and Supplementary Figs S3(d), S4(d), respectively.

Conclusion

This study conducted a numerical investigation on the impact of nonlinear thermal radiation, heat generation/absorption and magnetohydrodynamics (MHD) on the flow of Casson nanofluids (Ag/H_2O and CuO/H_2O) in a semi-porous channel. The Runge-Kutta (RK) method combined with the shooting technique was employed to solve the governing equations and MATLAB was used to generate graphical representations of the numerical solutions. The key findings of the study are as follows:

- Increasing the Casson fluid parameter (β_c) and the porosity parameter (K_r) leads to a reduction in the velocity profile and an increase in the temperature distribution.
- As M increases, the velocity profile decreases, while the temperature profile increases. The velocity profile reduces due to the influence of the Lorentz force, which opposes fluid motion.
- Increasing the nanoparticle volume fraction **(ϕ)** leads to a higher temperature profile and an expanded thermal boundary layer**.**
- An increase in both the nanoparticle volume fraction (ϕ) and the Casson fluid parameter (β_c) results in a decrease in friction drag and heat transfer**.**
- An increase in the Hartmann number (M) and the heat generation/absorption parameter results in a decrease in heat transfer at the surface of the channel.
- Enhancing the nanoparticle volume fraction in cooling systems optimizes thermal boundary layer management, ensuring efficient heat dissipation and preventing overheating in high-performance electrical circuits.
- Several key factors are considered when designing the dataset for the ANN-LM technique: (i) The ANN-LM model achieves R-values close to one across all response variables, indicating strong predictive performance. (ii) The study results confirm that the developed ANN-LM model exhibits high accuracy in predicting skin friction coefficients and the Nusselt number**.**
- The optimal validation performance for the Nusselt number and skin friction in the MHD flow of Casson nanofluids (*Ag/H_2O* and *CuO/H_2O*) was achieved with Nusselt number values of 0.03981 at epoch 5 and 0.0013162 at epoch 4, while skin friction values were 0.010651 at epoch 6 and 0.031524 at epoch 2, respectively.
- Future work can expand upon these findings by exploring variable magnetic fields, hybrid nanofluids and AI-driven predictive models to enhance heat transfer performance further. These advancements can drive innovations in electronics cooling, renewable energy systems and biomedical engineering.

Supplementary Information

Supplementary information is available on the website http://nopr.niscpr.res.in/handle/123456789.

Conflict of interest

The authors declare no conflict of interest.

Nomenclature

ν	kinematic viscosity $[m^2s^{-1}]$	β_c	the Casson fluid parameter
g	acceleration due to gravity $[\mathrm{ms}^{-2}]$	ρ	density of the fluid $[kgm^3]]$
C_p	the specific heat at constant pressure $[\mathrm{JK}^{-1}\mathrm{Kg}^{-1}]$	μ_f	fluid viscosity $[Nm^{-2}s^{-1}]]$
q_r	the radiative flux$[W]$	σ	the electrical conductivity of the fluid $[Wm^{-1}K^{-1}]$
k^*	the coefficient of heat absorption $[JK^{-1}]$	σ^*	the Stefan-Boltzmann constant $[Wm^{-1}K^{-1}]$
Pr	the Prandtl number	τ_e	the collision time of electron
N	the thermal radiation parameter	θ	dimensionless temperature
H_T	the heat generation/ absorption parameter	w	conditions at the wall
K_r	the porosity parameter	∞	free stream conditions
M	the Hartmann number	nf	nanofluid
Nu	dimensionless Nusselt number	f	basefluid
ϕ	volume fraction of *Ag* or *CuO* nanoparticles		

References

1 Choi S U & Eastman J A, Enhancing thermal conductivity of fluids with nanoparticles, (No. ANL/MSD/CP-84938; CONF-951135-29), Argonne National Lab, Argonne, IL (United States) (1995).

2 Wang X Q & Mujumdar A S, A review on nanofluids-part II: Experiments and applications, *Braz J Chem Eng*, 25 (2008) 631.

3 Wen D, Lin G, Vafaei S & Zhang K, Review of nanofluids for heat transfer applications, *Particuology*, 7 (2009) 141.

4 Wong K V & De-Leon O, Applications of nanofluids: Currentand future, *Adv Mech Eng*, 2 (2010) 519659.

5 Saidur R, Leong K Y & Mohammed H A, A review on applications and challenges of nanofluids, *Renew Sustain Energy Rev*, 15 (2011) 1646.

6 Dash R K, Mehta K N & Jayaraman G, Casson fluid flow in a pipe filled with a homogeneous porous medium, *Int J Eng Sci*, 34 (1996) 1145.

7 Khan M, Irfan M, Khan W A & Alshomrani A S, A new modeling for 3D Carreau fluid flow considering nonlinear thermal radiation, *Results Phys*, 7 (2017) 2692.

8 Khan H, Haneef M, Shah Z, Islam S, Khan W & Muhammad S, The combined magneto hydrodynamic and electric field effect on an unsteady Maxwell nanofluid flow over a stretching surface under the influence of variable heat and thermal radiation, *Appl Sci*, 8 (2018) 160.

9 Khan M I, Hayat T, Khan M I & Alsaedi A, A modified homogeneous-heterogeneous reactions for MHD stagnation flow with viscous dissipation and Joule heating, *Int J Heat Mass Transf*, 113 (2017) 310.

10 Durairaj M, Ramachandran S & Mehdi R M, Heat generating/absorbing and chemically reacting Casson fluid flow over a vertical cone and flat plate saturated with non-Darcyporousmedium, *Int J Numer Method Heat Fluid Flow*, 27 (2017) 156.

11 Mukhopadhyay S, Effect of thermal radiation on unsteady mixed convection flow and heat transfer over a porous stretching surface in porous medium, *Int J Heat Mass Transf*, 52 (2009) 3261.

12 Chamkha A J, Hydromagnetic combined convection flow in a verticallid-driven cavity with internal heatgeneration or absorption, *Numer Heat Transf Part A: Appl*, 41 (2002) 529.

13 Saleem S, Al-Qarni M M, Nadeem S & Sandeep N, Convective heat and mass transfer in magneto Jeffrey fluid flow on a rotating cone with heat source and chemical reaction, *Commun Theor Phys*, 70 (2018) 534.

14 Sheikholeslami M, Bandpy M G, Ellahi R & Zeeshan A, Simulation of MHD CuO water nanofluid flow and convective heat transfer considering Lorentz forces, *J Magn Magn Mater*, 369 (2014) 69. Gireesha B J, Archana M, Mahanthesh B & Prasannakumara B C, Exploration of activation energy and binary chemical reaction effects on nano Casson fluid flow with thermal and exponential space-based heat source, *Multidiscip Model Mater Struct*, 15 (2018) 227.

15 Dharmaiah G, Baby R C H, Vedavathi N & Balamurugan K S, Hall and ion slip effects on Ag-water based MHD nanofluid flow over a semi-infinite vertical plate embedded in a porous medium, *Front in Heat Mass Transf*, (2020) 14.

16 Nouri R, Ganji D D & Hatami M, MHD nanofluid flow analysis in a semi-porous channel by a combined series solution method, *Chall Nano Micro Scale Sci Technol*, 1 (2013) 124.

17 Aghalya T, Tamizharasi R & Muthuchamy N, Channel with Cu-H_2O nanofluid in interplay of fractals and complexity in mathematical modelling and physical patterns: Selected proceedings of the international symposium on mathematical analysis of fractals and dynamical systems-2023 (ISMAFDS-2023), *Springer Nature*, (2025) 195.

18 Varatharaj K & Tamizharasi R, Nonlinear thermal radiation effect on magnetohydrodynamics flow of Cu-H_2O and TiO_2-H_2O of Casson nanofluids over stretching wall through porous channel, *Int J Mod Phys B*, 37 (2003) 2350296.

19 Raja M A Z, Shoaib M, Khan Z, Zuhra S, Saleel C A, Nisar K S & Khan I, Supervised neural networks learning algorithm for three dimensional hybrid nanofluid flow with radiative heat and mass fluxes, *Ain Shams Eng J*, 13 (2022) 101573.

20 Toghraie D, Sina N, Jolfaei N A, Hajian M & Afrand M, Designingan artificial neural network (ANN) to predict the viscosity of Silver/Ethylene glycol nanofluid at different temperatures and volume fraction of nanoparticles, *Phys A: Stat Mech Appl*, 534 (2019) 122142.

21 Akhgar A, Toghraie D, Sina N & Afrand M, Developing dissimilar artificial neural networks (ANNs) to prediction the thermal conductivity of MWCNT-TiO_2/Water-ethylene glycol hybrid nanofluid, *Powder Technol*, 355 (2019) 602.

22 Kumar K A, Sakkaravarthi K & Reddy P B A, Levenberg-marquardt neural network for entropy optimization on Casson hybrid nanofluid flow with nonlinear thermal radiation: A comparative study, *Eur Phys J Plus*, 139 (2024) 555.

23 Rosseland S, Astrophysik and atom-theoretische grundlagen, Berlin: Springer Verlag, (1931).

24 Khanafer K, Vafai K & Lightstone M, Buoyancy-driven heat transfer enhancement in a two-dimensional enclosure utilizing nanofluids, *Int J Heat Mass Transf*, 46 (2003) 3639.

25 Brinkman H C, The viscosity of concentrated suspensions and solutions, *J Chem Phys*, 20 (1952) 571.

26 Maxwell J C, A treatise on electricity and magnetism, Oxford: clarendon press, 1 (1873).

27 Sumalatha C & Bandari S, Effects of radiations and heat source/sink on a Casson fluid flow over nonlinear stretching sheet, *World J Mech*, 5 (2015) 257.

28 Abd-El A M, Viscous dissipation effect on mixed convection flow of a micropolar fluid over an exponentially stretching sheet, *Can J Phys*, 87 (2009) 359.

29 Ishak A, Nazar R & Pop I, Mixed convection boundary layer flow adjacent to a vertical surface embedded in a stable stratified medium, *Int J Heat Mass Transf*, 51 (2008) 3693.

30 Pramanik S, Casson fluid flow and heat transfer past an exponentially porous stretching surface in presence of thermal radiation, *Ain Shams Eng J*, 5 (2014) 205.

31 Aghalya T & Tamizharasi R, Unsteady MHD casson nanofluid flow pastan exponentially accelerated vertical plate: An analytical strategy, *Comput Model Eng Sci*, 140 (2024) 431.

32 Raza J, Rohni A M & Omar Z, MHD flow and heat transfer of Cu-water nanofluid in a semi porous channel with stretching walls, *Int J Heat Mass Transf*, 103 (2016) 336.

33 Manohar B, Das R, Lakshmi M, Prajapati J I & Reddy K M, Artificial neural network-based stock price prediction using Levenberg-Marquardt algorithm, *Artif Intell Solut Indust Appl*, (2024) 315.

34 Manohar B & Das R, Artificial neural networks for prediction of COVID-19 in India by using backpropagation, *Expert Syst*, 40 (2023) e13105.

35 Manohar B & Das R, Comparison of hybrid artificial neural networks with GA, PSO, and RSA in predicting COVID-19 cases: A case study of India, multi-disciplinary applications of fogcomputing: Responsivenessinreal-time, IGI Global Scientific Publishing (2023) 207.

36 Sakkaravarthi K, Reddy P B A & Sakthi I, Entropy optimization in Casson tetra-hybrid nanofluid flow over a rotating disk with nonlinear thermal radiation: A Levenberg-Marquardt neural network approach, *J Comput Des Eng*, 11 (2024) 333.

37 Divya A, Reddy P B A & Das R, Entropy optimization of non-Newtonian hybrid nanofluid EMHD flow by numerical and Levenberg-Marquardt backpropagation approach over a rotating disk, *Waves Random Complex Media*, (2023) 1.

38 Kumar M, Kaswan P & Kumari M, Entropy generation analysis of microrotating Casson's nanofluid with Darcy-forchheimer porous media using a neural computing based on Levenberg- Marquardt algorithm, *Int J Numer Meth Heat Fluid Flow*, 34 (2024) 2285.

40 Ali A, Ahamma N A, Tag-Eldin E, Gamaoun F, Daradkeh Y I & Yassen M F, MHD Williamson nanofluid flow in the rheology of thermal radiation, Joule heating, and chemical reaction using the Levenberg-Marquardt neural network algorithm, *Front Energy Res*, 10 (2022) 965603.